

Cumulative representations of these parameters can be defined as a function of time or test parameter (such as pressure or temperature), including: (1) total hits, (2) amplitude distribution and (3) accumulated energy. Once a specific parameter is selected, rate functions may be defined as a function of time or test parameter: hit rate, count rate or energy rate.

Based on Fig. 7, several techniques for characterizing acoustic emission are described below.

## Waveform Parameters

### Emission Hits and Count

Acoustic emission hits are individual signal bursts produced by local material changes. The hit count is the number of times a signal crosses a preset threshold. High amplitude hits of long duration tend to have many threshold crossings. The number of threshold crossings per unit time depends on (1) the transducer frequency, (2) the damping characteristics of the transducer, (3) the damping characteristics of the structure and (4) the threshold level.

The idealized signal in Fig. 5 can be represented by Eq. 1:<sup>19</sup>

$$(1) \quad V = V_0 e^{-Bt} \sin \omega t$$

where  $B$  is the decay constant (greater than 0),  $e$  is the root of natural logarithms,  $t$  is time (second),  $V$  is the output potential (volt) of the transducer,  $V_0$  is the initial signal amplitude and  $\omega$  is angular frequency (radian per second).

A common way to measure acoustic emission activity is by ringdown counts, the number of times the transducer signal exceeds a counter threshold. When the time  $t$  required for the signal to decay to the threshold voltage  $V_t$  is long compared

to the period of oscillation, then the number of counts  $N$  from a given hit can be given:

$$(2) \quad N = \frac{\omega}{2\pi B} \ln \frac{V_0}{V_t}$$

where  $V_t$  is the threshold potential (volt) of the counter.

### Correlation of Count Rate and Material Properties

As shown in Fig. 7, a single acoustic emission hit can produce several counts. A larger hit requires more cycles to ring down to the trigger level and will produce more counts than a smaller hit. This provides a measure of the intensity of the acoustic emission hit.

Correlations have been established between total counts, count rate and various fracture mechanics parameters (such as stress intensity factor)<sup>20-25</sup> as expressed in Eq. 3 or fatigue crack propagation rate<sup>22-25</sup> as expressed in Eq. 4:

$$(3) \quad N \cong K^n$$

where  $K$  is the stress intensity factor,  $N$  is the total number of counts and  $n$  is a constant with a value between 2 and 10.

$$(4) \quad \frac{dN}{dc} \cong \frac{da}{dc}$$

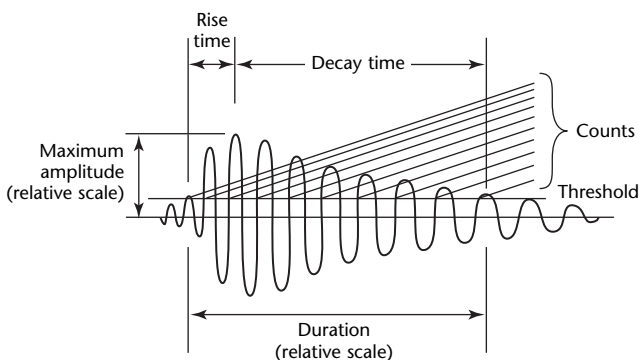
where  $a$  is the crack size,  $c$  is the number of cycles and  $N$  is the total number of counts.

The counts are a complex function of the frequency response  $\omega$  of the transducer and the structure, the damping characteristics of the transducer, the hit and the propagation medium  $B$ , signal amplitude, coupling efficiency, transducer sensitivity, amplifier gain and the threshold voltage  $V_t$ . Maintaining stability of these parameters throughout a test or from test to test is difficult but essential for consistency of interpretation. Nevertheless, counts are widely used as a practical measure of acoustic emission activity.

### Acoustic Emission Event Energy

Because acoustic emission activity is attributed to the rapid release of energy in a material, the energy content of the acoustic emission signal can be related to this energy release<sup>26,27</sup> and can be measured in several ways. The true energy is directly proportional to the area under the acoustic emission waveform. The electrical energy  $U$  present in a transient hit can be defined as:

FIGURE 7. Definition of simple waveform parameters.



wave. The angle of the reflected longitudinal wave  $\theta_{rl}$  is 1.57 rad (90 deg) when Eq. 68 is satisfied:

$$(68) \quad \theta_i = \arcsin \frac{c_2}{c_1} = \theta_c$$

This value of the incident angle is called the *critical angle*. At this angle, the transverse wave is the only wave reflected back into the medium. The longitudinal wave, which is apparently reflected parallel to the surface, actually has a vanishingly small amplitude away from the free surface. That component can be shown to be equivalent to a disturbance propagating at the same speed as the intersection of the two transverse waves along the surface. For angles greater than  $\theta_c$ , the incident transverse wave is totally reflected into the medium.

If the displacement amplitude of the incident transverse wave is unity, the amplitudes of the two reflected waves are as follows:

$$(69) \quad A_{rt} = \frac{\sin(2\theta_i)\sin(2\theta_{rl}) - \kappa^2 \cos^2(2\theta_i)}{\sin(2\theta_i)\sin(2\theta_{rl}) + \kappa^2 \cos^2(2\theta_i)}$$

$$(70) \quad A_{rl} = \frac{\kappa \sin(4\theta_i)}{\sin(2\theta_i)\sin(2\theta_{rl}) + \kappa^2 \cos^2(2\theta_i)}$$

where  $\kappa = c_1 \cdot c_2^{-1}$  is the ratio of the speed of longitudinal waves to the speed of transverse waves.

If  $\theta_i$  is less than  $\theta_c$ , then Eqs. 69 and 70 are simple and well behaved. If the angle of the incident transverse wave is greater than the critical angle  $\theta_c$ , then the two equations change character and become complex functions of the incident angle and the wave speed ratio. If  $\theta_i$  is greater than  $\theta_c$ , then Eqs. 69 and 70 reduce to the following forms:

$$(71) \quad A_{rt} = e^{j2\alpha}$$

$$(72) \quad A_{rl} = S e^{j\alpha}$$

The values of  $S$  and  $\alpha$  are determined below:

$$(73) \quad S = \kappa \sin(4\theta_i) + \left\{ \kappa^2 \cos^4(2\theta_i) + 4 \left[ \kappa^2 \sin^2(\theta_i) - 1 \right] \times \sin^2(2\theta_i) \sin^2(\theta_i) \right\}^{-2}$$

$$(74) \quad \tan \alpha = \left[ 2 \sqrt{\kappa^2 \sin^2(\theta_i) - 1} \times \sin(2\theta_i) \sin(\theta_i) \right] + \kappa \cos^2(2\theta_i)$$

In this case, the expressions for the reflected waves are as follows:

$$(75) \quad u_1^{rt} = \alpha_2 e^{j[k_2(\alpha_1 x_1 - \alpha_2 x_2) - \omega t - 2\alpha]}$$

$$(76) \quad u_2^{rt} = \alpha_1 e^{j[k_2(\alpha_1 x_1 - \alpha_2 x_2) - \omega t - 2\alpha]}$$

$$(77) \quad u_1^{rl} = \beta_1 S e^{\zeta x_2} e^{j(k_2 \beta_1 x_1 - \omega t - \alpha)}$$

$$(78) \quad u_2^{rl} = \beta_2 S e^{\zeta x_2} e^{j(k_2 \beta_1 x_1 - \omega t - \alpha)}$$

The terms  $\alpha_1$  and  $\alpha_2$  in Eqs. 75 and 76 are the direction cosines of the reflected transverse waves and are given by the expressions  $\alpha_1 = \sin \theta_i$  and  $\alpha_2 = \cos \theta_i$ . The terms  $\beta_1$  and  $\zeta$  in Eqs. 77 and 78 are determined from  $\beta_1 = \kappa \sin \theta_i$ ,  $\beta_2 = j\zeta$  and  $\zeta = (\kappa^2 \sin^2 \theta_i - 1)$ .

With the angles of incidence  $\theta_i > \theta_c$ , the amplitude of the reflected transverse wave is equal to the amplitude of the incident transverse wave but the phase of the reflected transverse wave is shifted by  $2\alpha$ . The other term (Eqs. 77 and 78) was a reflected longitudinal wave for  $\theta_i < \theta_c$ . However, for  $\theta_i > \theta_c$ , it is no longer a plane wave traveling into the medium but rather is a heterogeneous disturbance propagating along the surface at the same speed as the projection of the transverse wave along the surface.

Plots of Eqs. 69 and 70 (or for  $\theta_i > \theta_c$ , Eqs. 71 and 72) are shown in Fig. 35. Note that, as the incident angle increases from zero, the magnitude of the reflected transverse wave decreases whereas the amplitude of the reflected longitudinal wave increases. In this region, the incident transverse wave is increasingly converted to a longitudinal wave as the incident angle increases up to about 0.5 rad (30 deg). At this incident angle, the amplitude of the reflected transverse wave begins to increase.

The discontinuity in Fig. 35 occurs at the critical angle, 0.564 rad (32.3 deg) for Poisson's ratio of 0.3. For angles greater than the critical, the amplitude of the reflected transverse wave is equal to the amplitude of the incident transverse wave but the phase of the reflected wave changes as discussed above. The amplitude of the reflected longitudinal

(1) are large in number, (2) are distributed uniformly in orientation and (3) are uncorrelated with respect to phase. Such a wave field is called a *diffuse wave field*. For sound waves in fluids, this concept gives rise to a branch of acoustics called *geometric acoustics*.<sup>141</sup>

### Diffuse Wave Field Equations

Using the assumptions given above and neglecting contributions from surface waves, it can be shown<sup>142</sup> that the time average of the acoustic energy per unit volume (energy density) is:

$$(116) \quad \xi = \xi_1 + \xi_2$$

where  $\xi_1$  and  $\xi_2$  are energy densities (joule per cubic meter) of the longitudinal and transverse waves respectively. It can further be shown that each of these energy densities is independent of position in the medium. The equations of motion of the medium (assumed to be homogeneous and isotropic) then reduce:

$$(117) \quad V \ddot{\xi}_1 + \frac{1}{4} \gamma_{12} S c_1 \xi_1 - \frac{1}{4} \gamma_{21} S c_2 \xi_2 = P_1$$

and:

$$(118) \quad V \ddot{\xi}_2 + \frac{1}{4} \gamma_{21} S c_2 \xi_2 - \frac{1}{4} \gamma_{12} S c_1 \xi_1 = P_2$$

The terms  $P_1$  and  $P_2$  are the acoustic powers generated by the source in the form of longitudinal and transverse waves respectively. The terms  $\gamma_{12}$  and  $\gamma_{21}$  are the diffuse field power reflection coefficients (defined as the fraction of incident diffuse field longitudinal or transverse wave power converted to transverse or longitudinal waves caused by mode conversion at the boundary of the medium). The terms  $\xi_1$  and  $\xi_2$  are the time averaged energy densities of longitudinal and transverse waves respectively.

Equations 117 and 118 show that the longitudinal and transverse wave fields generated by the source exist independently, except for the mode conversion that occurs at the boundaries of the medium. The coefficients  $\gamma_{12}$  and  $\gamma_{21}$  determine the extent of the interaction of the two wave types. If the surface of the medium is entirely free, then these coefficients can be calculated by the following integrals:

$$(119) \quad \gamma_{12} = \frac{\int P_{rt} d\Omega}{\int P_{il} d\Omega}$$

and:

$$(120) \quad \gamma_{21} = \frac{\int P'_{tl} d\Omega}{2 \int P_{it} d\Omega}$$

where  $P_{il}$ ,  $P_{rt}$ ,  $P_{it}$  and  $P'_{tl}$  are given by Eqs. 87 to 91.

The integrations in Eqs. 119 and 120 are over the solid angle  $\Omega$  (steradian), where  $\Omega = 2\pi$  sr. The factor 2 in the denominator of the second equation results from the fact that *SH* waves are reflected unchanged from the free surface. The integrals are a function of Poisson's ratio  $\nu$  and can be evaluated numerically. Results for selected values of  $\nu$  are given in Table 10.

### Diffuse Field Solution for Impulsive Sources

Consider a source that releases a finite quantity of energy instantaneously at  $t = 0$ . The subsequent energy densities can be determined by setting  $P_1$  and  $P_2 = 0$  and solving Eqs. 117 and 118 subject to these initial conditions:  $\xi_1(0) = E_1 \cdot V^{-1}$  and  $\xi_2(0) = E_2 \cdot V^{-1}$ . The terms  $E_1$  and  $E_2$  are the longitudinal and transverse energies released by the source. The solutions to Eqs. 117 and 118 are:

$$(121) \quad \xi_1(t) = K_1 + K_2 \exp\left(-\frac{t}{t^*}\right)$$

and:

**TABLE 10. Diffuse field mode conversion power coefficients for selected values of Poisson's ratio.**

$\nu$	$\gamma_{12}$	$\gamma_{21}$
0.00	0.601	0.150
0.05	0.650	0.153
0.10	0.708	0.156
0.15	0.761	0.155
0.20	0.789	0.145
0.25	0.769	0.128
0.30	0.686	0.098
0.35	0.536	0.062
0.40	0.337	0.028
0.45	0.131	0.006
0.50	0.000	0.000

tested with each of the two schemes. The solid lines in Fig. 27 indicate pressurization and acoustic emission test data being considered simultaneously, whereas the broken or dashed lines indicate pressurization data only.

Historically, some of the thinking behind the load-hold-unload pressurization scheme has been to measure the felicity effect<sup>27,32</sup> and to research the creep behavior during the hold periods.<sup>16,26,27,31</sup> In this case, the two different loading sequences were used to observe the bottles at different loading rates and load levels. The low pressure ramp holds were also designed to see if

the acoustic emission test data would provide meaningful results at about 25 percent of the anticipated burst pressure and whether or not the additional proof cycle provided by the ramp-hold-unload scheme would significantly reduce the burst pressures.

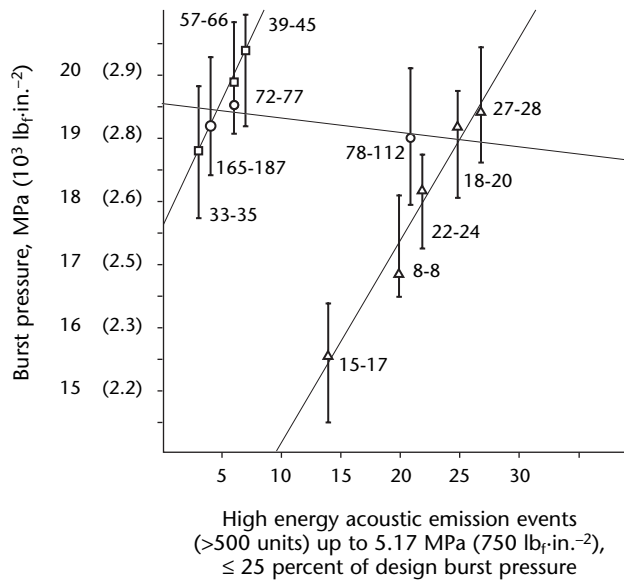
## Results

The acoustic emission test data from the first fiberglass epoxy bottle<sup>24,25,33</sup> were of no use because the thresholds for the four acoustic emission analyzer channels were set too low and the pressurization rate was too high. Consequently, the event rate was so large that the acoustic emission analyzer was unable to distinguish one event from the next and the output was recorded as one continuous event rather than a series of discrete events. The thresholds were subsequently increased to 60 dB and the pressurization rate was reduced to  $70 \text{ MPa}\cdot\text{s}^{-1}$  ( $600 \text{ lb}_f\cdot\text{in.}^{-2}\cdot\text{min}^{-1}$ ). This allowed the internal microprocessor to operate just below its saturation point, which was about 40 hits per second per channel.

Figure 28 is a plot of burst pressure versus high energy acoustic emission events (more than 500 counts) up to  $5.17 \text{ MPa}$  ( $750 \text{ lb}_f\cdot\text{in.}^{-2}$  gage), 25 percent of the design burst pressure, for the remaining 11 bottles. The low temperature data points are indicated by the hollow squares and the room temperature data points are plotted as triangles.

A multiple linear regression analysis was performed using the variables listed in Table 4 to find a burst pressure prediction equation. The number of high energy acoustic emission events is a continuous variable and, as such, was represented by the appropriate numerical values for each bottle; the dummy variables 0 and 1 were used to describe the pressurization scheme, the burst

**FIGURE 28.** Burst pressure versus high energy acoustic emission events for 146 mm (5.75 in.) diameter bottles.



### Legend

- = 0 °C (32 °F)
- △ = 21.1 °C (70 °F)
- = 43.3 °C (110 °F)

**TABLE 4.** Variables in multiple-regression analysis for 146 mm (5.75 in.) diameter bottles.

Variable Class	Specific Variable	Detail	Value
Dependent (continuous)	burst pressure (BP)		—
Independent (continuous)	high energy acoustic emission events (HEE)		—
Independent (categorical)	pressurization scheme (PS)	load-hold-unload	1
		ramp to failure	0
		transducer configuration (XDCR)	four transducers
		two transducers	0
	burst temperature (T1 and T2)	273.2 K = 0 °C = 32 °F	0, 0
		294.3 K = 21.1 °C = 70 °F	1, 0
		316.5 K = 43.3 °C = 110 °F	0, 1

temperature and the transducer configuration because these are categorical variables.<sup>29</sup> Numerical values were not assigned to the manufacturing discontinuities because it was assumed that their effect would be manifested in either an increase or a decrease in the number of high energy acoustic emission events. The data used in the linear regression are summarized in Table 5.

The multiple-regression analysis was carried out in stepwise fashion to determine the statistical significance of each of the independent variables to the overall prediction equation. This was accomplished using a software subroutine. Having thus determined the most significant variables, the following burst pressure equation was obtained from another subroutine:

$$(3) \text{ BP} = 17.65 + 0.385 \text{ HEE} \\ - 6.63 \text{ T1} + 1.83 \text{ T2} \\ - 0.070 \text{ HEE} * \text{T1} - 0.408 \text{ HEE} * \text{T2}$$

where HEE indicates high energy events and T1 and T2 indicate values for categorical variables describing the first and second transducer configuration, respectively.

It was necessary to use Eq. 2 because there was an interaction between the temperature and the number of high energy events sensed by the transducer — that is, temperature affected the output of the piezoelectric transducers. Inputting a value of 0 for the categorical variable T1 and a value of 0 for T2 yields the equation for the 0 °C (32 °F) straight line in the upper left corner of Fig. 28; inputting a 1 for T1 and a 0 for T2 gives the 21.1 °C (70.0 °F) line; inputting a 0 for T1 and a

1 for T2 produces the 43.3 °C (110 °F) line. It can be seen that Eq. 3 includes the two bottles (15-17 and 8-8) with simulated manufacturing discontinuities and that these discontinuities did indeed produce a marked drop in the burst pressure. Also, among the bottles without discontinuities, the burst pressures were not significantly reduced by the additional pressurization ramp in the load-hold-unload scheme (as opposed to the straight ramp to failure).

The sample standard deviation for regression is  $s = 288 \text{ kPa}$  (41.8 lb<sub>f</sub>-in.<sup>-2</sup>) and the multiple-correlation coefficient adjusted for degrees of freedom is  $R^{*2} = 95.8$  percent. This says that 95.8 percent of the variability in the burst pressure is accounted for by the prediction equation. For a worst case 95 percent prediction interval, the burst pressure can still be predicted to within  $\pm 0.1046 \text{ MPa}$ . The predicted values and the 95 percent prediction intervals are shown for each point on the plot (Fig. 28).

Additional tests were performed on six 457 mm (18 in.) diameter bottles. The results were consistent with those for the 146 mm (5.75 in.) diameter bottles and are reported elsewhere.<sup>24</sup>

## Conclusions

Several conclusions result from the acoustic emission tests of fiberglass epoxy bottles.

1. A single-regression equation, derived from the 11 fiberglass epoxy bottles, is capable of predicting burst pressures to an accuracy of  $\pm 4.35$  percent. It has three independent variables: the number of high energy acoustic emission events, a continuous variable and the temperature at burst defined by the categorical variables T1 and T2. Thus, the number of high energy acoustic emission events provides a measure of the structural integrity and the burst temperature is a categorical identifier.
2. The regression equation included the effect of one type of manufacturing discontinuity, namely, premature hoop reversals. This effect was reflected in a decrease in the number of high energy acoustic emission events, consistent with the notion that delaminations relieve stress in such a way that the pressure vessel strength is increased.<sup>25</sup> Consequently, the more delaminations (high energy acoustic emission events) that occur during proof loading, the more uniform the stress field in the bottle and the higher the burst pressure.

TABLE 5. Data in multiple-regression analysis for 146 mm (5.75 in.) diameter bottles.

Bottle Number	Burst Pressure	High Energy Event	Pressure Scheme	Transducer Configuration	
				T1	T2
15-17 <sup>a</sup>	15.56	14	1	1	0
8-8 <sup>a</sup>	16.85	20	1	1	0
22-24	18.17	22	1	1	0
18-20	19.11	25	1	1	0
27-28	19.41	27	1	1	0
33-35	18.82	3	0	0	0
165-187	19.22	4	0	0	1
72-77	19.53	6	0	0	1
57-66	19.90	6	0	0	0
39-45	20.39	7	0	0	0
78-112	18.98	21	0	0	1

a. Simulated manufacturing discontinuities.